sustainability

MDPI

Article

Analysis of Dynamic Behavior of Gravity Model Using the Techniques of Road Saturation and Hilbert Curve Dimensionality Reduction

Liumeng Yang, Ruichun He *, Jie Wang, Hongxing Zhao and Huo Chai

School of Traffic and Transportation, Lanzhou Jiaotong University, Lanzhou 730070, China
* Correspondence: tranman@163.com

Abstract: In this study, we investigate the relationship between parameters and the dynamic behavior of traffic flow in road traffic systems, and we propose a segmented cost function to describe the effects of this flow on the dynamic gravity model at different saturation levels. We use single-parameter bifurcation analysis, maximum Lyapunov exponent calculation, and three-parameter bifurcation analysis to reveal the effects of parameter variations on the nonlinear dynamical behaviors of the modified gravity model, and we investigate the evolution laws of the traffic system in depth. In order to solve the problems of low efficiency and poor visualization ability in traditional dynamics analysis techniques, this paper proposes the Hilbert curve dimensionality reduction technique, which can completely retain the original data features. The three-dimensional pseudo-Hilbert curve is used to traverse the three-parameter bifurcation data, realizing the transformation of data from three- to one-dimensional. Then, the two-dimensional pseudo-Hilbert curve is used to traverse the reduced one-dimensional data, and the two-dimensional visualization of the three-parameter bifurcation diagram is successfully realized. The dimensionality reduction technique provides a new way of thinking for parameter analysis in the engineering field. By analyzing the two-dimensional bifurcation plan obtained after this reduction, it is found that the modified gravity model is more stable compared with the original model, and this conclusion is also verified by the wavelet transform results. Finally, a new robustness evaluation index is defined based on the dynamics of the model, and the simulation results reveal the intrinsic correlation between the saturation parameter and road congestion, which provides an important basis for promoting sustainable transportation in the road network.

Keywords: gravity model; saturation; fractals; chaos; Hilbert curve; robustness

check for updates

Citation: Yang, L.; He, R.; Wang, J.; Zhao, H.; Chai, H. Analysis of Dynamic Behavior of Gravity Model Using the Techniques of Road Saturation and Hilbert Curve Dimensionality Reduction. *Sustainability* **2024**, *16*, 5721. https://doi.org/10.3390/su16135721

Academic Editor: Lihui Zhang

Received: 22 April 2024
Revised: 23 June 2024
Accepted: 2 July 2024
Published: 4 July 2024

Copyright: © 2024 by the authors. Licensee MDPI, Basel, Switzerland. This article is an open access article distributed under the terms and conditions of the Creative Commons Attribution (CC BY) license (https://creativecommons.org/licenses/by/4.0/).

1. Introduction

Chaos dynamics is an important branch of complexity science that has evolved into a relatively comprehensive system after decades of development, and it has shown strong vitality across various fields, such as statistics [1], economics [2], aviation [3], ecology [4,5], and electronic circuits [6,7]. The transportation system is a large-scale and complex system with multifaceted nonlinear relationships among its elements, inevitably giving rise to chaotic phenomena [8–14]. For instance, vehicles frequently start and stop on busy roads, traffic accidents lead to congestion, and some city streets experience heavy traffic while others remain sparsely populated. The chaotic characteristics of the traffic system can be observed through the dynamic patterns of traffic flow, which remain unaffected by the time scale [15–17]. With the application of complex network and Bayesian theories in transportation, the time series prediction technology for traffic flow has made notable strides in recent years [18,19].

Newton's law of gravity inspired the development of gravity models, which provide a reliable mathematical method for modeling and analyzing transportation network problems [20]. Simini et al. used stochastic processes related to population distribution data to solve the problem of gravity models that depend on configurable parameters [21].

Hong et al. used a gravity model framework to study the traffic flow of a medium-sized city in South Korea [22]. In addition, Goh et al. revealed the Yule-type characteristics of Seoul's subway system using a Hill function augmented gravity model [23]. Wu et al. planned the transportation network of Nanliang town by incorporating topographical, political, and economic factors and used a gravity model to predict the occurrence, attraction, and distribution of traffic flows [24]. Asmael et al. used a gravity model to estimate the passenger flow of Baghdad's public transportation system to help urban decision making [25].

Classical gravity models are static and overlook the influence of road congestion. Consequently, these models must consider the time-varying nature of transportation systems. A dynamic gravity model with intricate dynamic characteristics was explored to address this issue [26]. However, when the original cost function fails to function effectively, such as in the case of road obstruction, the outcomes of this model may yield significant errors. In this study, we propose a cost function that integrates unsaturated, saturated, and oversaturated states to quantify the impact of actual traffic conditions on the gravity model.

The analysis of the dynamic behavior of chaotic systems typically employs technical methods, such as phase diagrams, bifurcation diagrams, and Poincaré cross-sections [27–30]. While these conventional methods can illustrate the system's evolution, they suffer from low efficiencies and visualization capabilities. When dealing with abundant parameters, the system operations demand significant computational power. Additionally, due to the sensitivity of initial values and the uncertainty of solutions in chaotic systems, previous prediction results may not directly apply to new environments when the system experiences minor perturbations. Consequently, generating new data becomes time-consuming. In the rapid development of big data, cloud computing, and intelligent systems, the traditional method of dynamical behavior analysis is inadequate in meeting the demands of rapid response and high visualization. A new approach is required for traffic managers to integrate traditional dynamical analysis techniques with the ongoing rapid advancements in intelligent transportation technology, thereby ensuring the sustainable operation of the transportation system. To address this challenge, we propose utilizing a three-parameter bifurcation analysis. However, as dimensionality escalates, data visualization decreases and the dynamics of three-parameter bifurcation diagrams become complex. Hence, the dimensionality reduction of high-dimensional data becomes essential.

Dimensionality reduction techniques are used to decrease the number or dimensionality of features in a high-dimensional dataset. They aim to retain the essential information of the data while simplifying the complexity and storage space requirements for enhanced data analysis, visualization, and model building [31–33]. Spatial dimensionality reduction techniques are commonly applied to handle datasets with numerous features, such as images, text, and bioinformatics data. However, traditional spatial dimensionality reduction techniques, such as principal component analysis, linear discriminant analysis, and stochastic projection, often struggle to maintain local continuity. Yet, the property of the Hilbert curve, which traverses all points in space without repetition and strives to maintain original point continuity as much as possible, can be utilized to address the discontinuity issue encountered in dimensionality reduction techniques. The Hilbert curve is a renowned space-filling curve in mathematics first proposed by German mathematician David Hilbert in 1890 [34–38]. It is a type of fractal curve with numerous intriguing properties widely employed in image processing, data compression, and computer graphics. Utilizing the Hilbert curve for dimensionality reduction in high-dimensional space can partially maintain the proximity and order of data points. This aids in comprehending the internal structure of the original data, consequently minimizing information loss when mapping high-dimensional data to low-dimensional space.

In the process of Hilbert curve dimensionality reduction, a set of one-dimensional time series with lengthy data is generated. In order to fully understand the characteristics of the data after dimensionality reduction, we introduce the wavelet transform, which is a signal processing technique often compared to a mathematical microscope that decomposes a signal into components of various scales and frequencies, facilitating a more detailed analysis in

both the time and frequency domains [39–42]. Distinguished from the Fourier transform, the wavelet transform utilizes elementary functions called wavelets, which are localized in both time and frequency. This attribute allows for superior adaptation to the non-stationary nature of signals. Consequently, it is highly suitable for analyzing low-dimensional time series derived from high-dimensional data, especially for nonlinear chaotic series.

The remainder of this paper is organized as follows. In Section 2, we introduce a gravity model with various dynamic characteristics. Section 3 proposes a cost function encompassing unsaturated, saturated, and oversaturated states. Section 4 presents the analysis of the dynamic characteristics of the corrective gravity model. Section 5 provides the Hilbert curve construction method. In Section 6, we reduce the dimensionality of the three-dimensional bifurcation data to generate a one-dimensional time series. Next, we apply the wavelet transform to the time series and then up-dimension this series to a two-dimensional Hilbert curve plane to obtain a low-dimensional three-parameter bifurcation diagram. In Section 7, we analyze the saturation parameters and develop a novel robustness evaluation index.

2. The Model

The dynamic gravity model is expressed as follows:

$$\begin{cases} F_{ij}(\mathbf{x}) = \psi_{ij}(\mathbf{x}) f(c(x_{ij})), \\ f(c(x_{ij})) = c(x_{ij})^{\mu} \exp(-\beta c(x_{ij})), \\ c(x_{ij}) = c_{ij}^{(0)}[1 + \alpha(x_{ij}/q_{ij})^{\gamma}]. \end{cases} \tag{1}$$

The parameters used are listed in Table 1. Discrete time is represented by n, and the OD flow pattern is denoted by $x(n)$. $\mathbf{x}(n+1) = F(\mathbf{x}(n))$. For the sake of clarity, we introduce the double-constrained gravity model (Model 1):

$$F_{ij}(\mathbf{x}) = a_i(\mathbf{x}) b_j(\mathbf{x}) f(c(x_{ij})),$$

$$x_{ij} \geq 0, \sum_i x_{ij} = d_j, \sum_j x_{ij} = o_i,$$

where

$$a_i(\mathbf{x}) = \frac{o_i}{\sum_j b_j(\mathbf{x}) f(c(x_{ij}))},$$

$$b_j(\mathbf{x}) = \frac{d_j}{\sum_i a_i(\mathbf{x}) f(c(x_{ij}))}$$

Subject to the initial state,

$$\mathbf{x}(0) = \begin{bmatrix} x_{11}(0) & x_{12}(0) \\ x_{21}(0) & x_{22}(0) \end{bmatrix} = \begin{bmatrix} 0.03 & 0.3521 \\ 0.5313 & 0.0866 \end{bmatrix} \tag{2}$$

and $\mu = 6.5$, $\alpha = 1$, $\beta = 3.25$, and $\gamma = 1$.

Table 1. Description of the parameters in (1).

Symbol	Meaning
x_{ij}	Number of overall trips made from zones i to j
$\mathbf{x}$	Trip matrix
$\psi_{ij}(\mathbf{x})$	Normalizing factor
$c(x_{ij})$	Total travel cost from zones i to j
$c_{ij}^{(0)}$	Travel cost of free flow from zones i to j
q_{ij}	The road's ability to accommodate traffic flows
$f(\cdot)$	Deterrence function
$\alpha, \beta, \gamma, \mu$	Constants

Note that an attractor is discovered and generated by the iteration of Model 1 (Figure 1). Nevertheless, the phase trajectories lack periodic properties and display intricate folding and stretching structures. This complex structure exhibits typical self-similarity and chaotic characteristics. The self-similarity of traffic flow mentioned above is related to the fractal nature of traffic flow, while long-term dependence is the origin of its formation and existence. Once the city layout and road network are determined, the overall travel characteristics of traffic flow on a particular road are also chosen despite minor random perturbations. In other words, the outflow characteristics of traffic flow exhibit a specific spatial and temporal long-term dependence or memory. This long-term dependence can result in an ordered spatiotemporal structure of traffic flow under certain conditions, such as fractal or chaotic conditions.

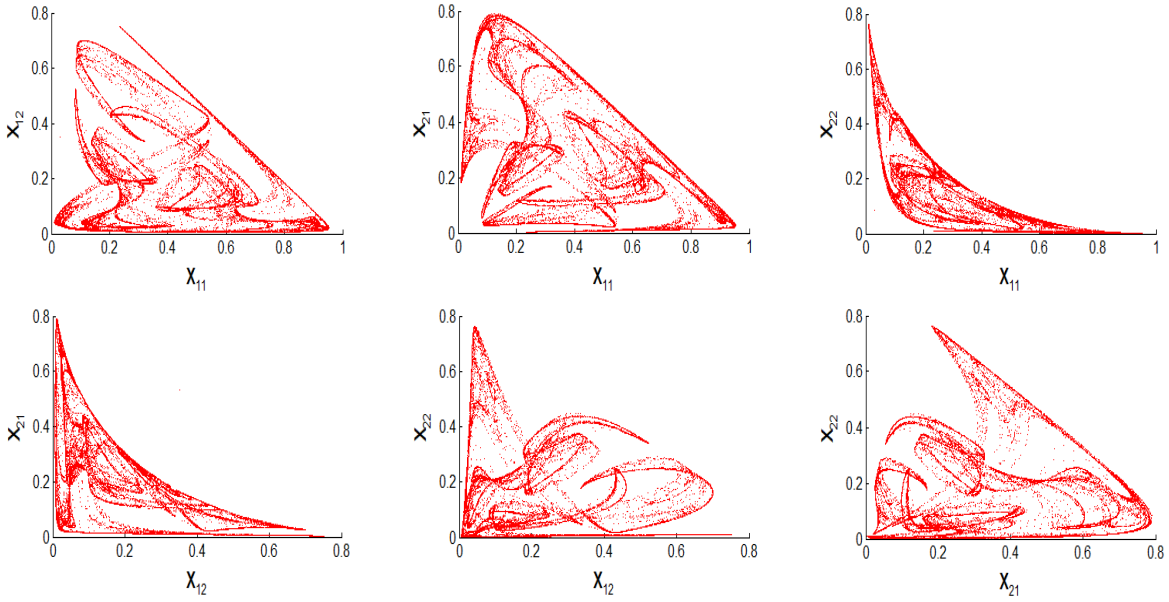


Figure 1. The chaotic attractor of Model 1.

3. Segmented Cost Function

3.1. Cost Function in the Unsaturated State

In cases where road traffic flow is low, the speed remains constant and unaffected by this flow [43]. Thus, if the degree of saturation $S_{ij} = x_{ij}/q_{ij}$ is lower than a certain threshold S_1, the travel cost is typically regarded as equal to the free travel cost, $c(x_{ij}) = c_{ij}^{(0)}$. Therefore,

$$c(S_{ij}) = \begin{cases} c_{ij}^{(0)}, & S_{ij} \in [0, S_1) \\ c_{ij}^{(0)}[1 + \alpha S_{ij}^{\gamma}], & S_{ij} \in [S_1, 1) \end{cases}.$$

3.2. Cost Function in the Saturated State

In cases of high traffic density, significant congestion occurs on the road. If this persists without mitigation, vehicle speeds will eventually decrease to zero, leading to the near-complete occupation of the road by vehicles. When traffic density surpasses the road's capacity limit, the actual traffic flow decelerates, exacerbating congestion. Therefore, the cost function

$$c(x_{ij}) = c_{ij}^{(0)}[1 + \alpha(x_{ij}/q_{ij})^{\gamma}]$$

becomes invalid. To address this issue, Wang's scheme is employed as the cost function to compute congestion [44]. For $S \in [1, S_2]$, the cost function is

$$c(y(x_{ij})) = c_{ij}^{(0)}[1 + \alpha(y(x_{ij}))^{\gamma}],$$

where S_2 denotes the threshold of the degree of saturation when obstruction occurs, and $y(x_{ij}) = 2 - S_{ij}$.

3.3. Cost Function in the Oversaturated State

The road network gravity model does not account for the fact that oversaturated traffic flow can easily lead to paralysis. Hence, for $S_{ij} \in [S_2, +\infty)$ exceeding the threshold, the traffic cost significantly rises, and the road resembles a parking lot. Due to the limited actual capacity of the road, the saturation eventually stabilizes at a high level. Let $y(x_{ij}) = M$, where M denotes the maximum saturation threshold, which is a positive value.

The new cost function is therefore defined as

$$c(S_{ij}) = c_{ij}^{(0)}[1 + \alpha(H(S_{ij}, 2 - S_{ij}, M)^T)^\gamma], \tag{3}$$

where H is a vector shown for different saturation states in Table 2.

Table 2. Vector H at different saturations.

Saturation	H
$S_{ij} \in [0, S_1)$	$(0, 0, 0)$
$S_{ij} \in [S_1, 1)$	$(1, 0, 0)$
$S_{ij} \in [1, S_2)$	$(0, 1, 0)$
$S_{ij} \in [S_2, +\infty)$	$(0, 0, 1)$

Substituting $c(x_{ij}) = c_{ij}^{(0)}[1 + \alpha(x_{ij}/q_{ij})^\gamma]$ with Equation (3) in Model 1, we derive the corrective gravity model (referred to as Model 2), where S_1, S_2, and M are the saturation parameters.

4. Analysis of Dynamic Characteristics of the Corrective Gravity Model

4.1. Analysis of Conventional Dynamical Behavior

In complex traffic scenarios, minor disturbances can propagate or be amplified along roads. To investigate this phenomenon, we used the bifurcation diagram, maximum Lyapunov exponent, and time series analysis. Here, we set $\alpha = 1$, β= 3.25, $\gamma = 1$, $S_1 = 0.022$, $S_2 = 1.8$, and $M = 3$ to generate the bifurcation diagram and maximum Lyapunov exponent diagram for Model 2, where $8.5 \leq \mu \leq 17.5$ and the origin is (2). The results are depicted in Figures 2 and 3, where Figure 3b,c,e,f,h,i are the partially magnified views of Figure 3a,d,g, respectively.

As depicted, for $u = 9$, the model is in a stable state and follows the orbit of period-1 (Figure 2a). When $u = 10.19$, the model exhibits the first bifurcation phenomenon and transitions from the orbits of period 1 to 2 (Figure 2a). Furthermore, in cases where $u = 12.88$, the model shifts from the orbits of period 2 to 4 (Figure 2a). This increase in parameter u gradually enhances the frequency of this period-doubling bifurcation. At $u = 13.70$, the model's topology undergoes a dramatic change, leading to chaotic behavior (Figure 3a). As illustrated in Figure 2, at $\mu \in [13.70, 13.82)$, the model exhibits chaotic motion. Upon closer inspection of Figure 2, periodic windows are observed within this chaotic region (Figure 3a,d,g). These periodic windows demonstrate a level of self-similarity characterized by alternating period-doubling bifurcation motion and chaotic motion (Figure 3). This self-similarity is a hallmark of fractals and evident in bifurcation diagrams due to the sensitivity of the gravity model's dynamic behavior to initial conditions. Even slight variations in the parameter μ may cause significant changes in the observed traffic behavior. In reality, abrupt vehicle movements or stops, as well as the actions of traffic officers, can profoundly impact the operation of an entire traffic network. When $u = 13.82$, the model's topology changes, transitioning from a chaotic state to period 4 motion (Figure 3a). Subsequently, the model enters a broader chaotic region through period-doubling bifurcation, a phenomenon repeated in the periodic window of nearly all subsequent chaotic regions. At $u = 17.07$, the model consistently exhibits chaotic behavior (Figure 3g).

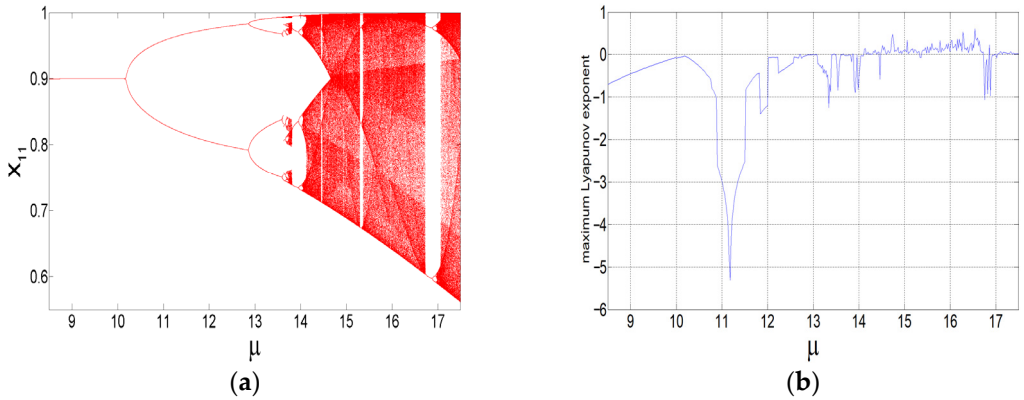


Figure 2. The analysis of the dynamic characteristics of Model 2: (**a**) single-parameter bifurcation diagram; (**b**) maximum Lyapunov exponent diagram.

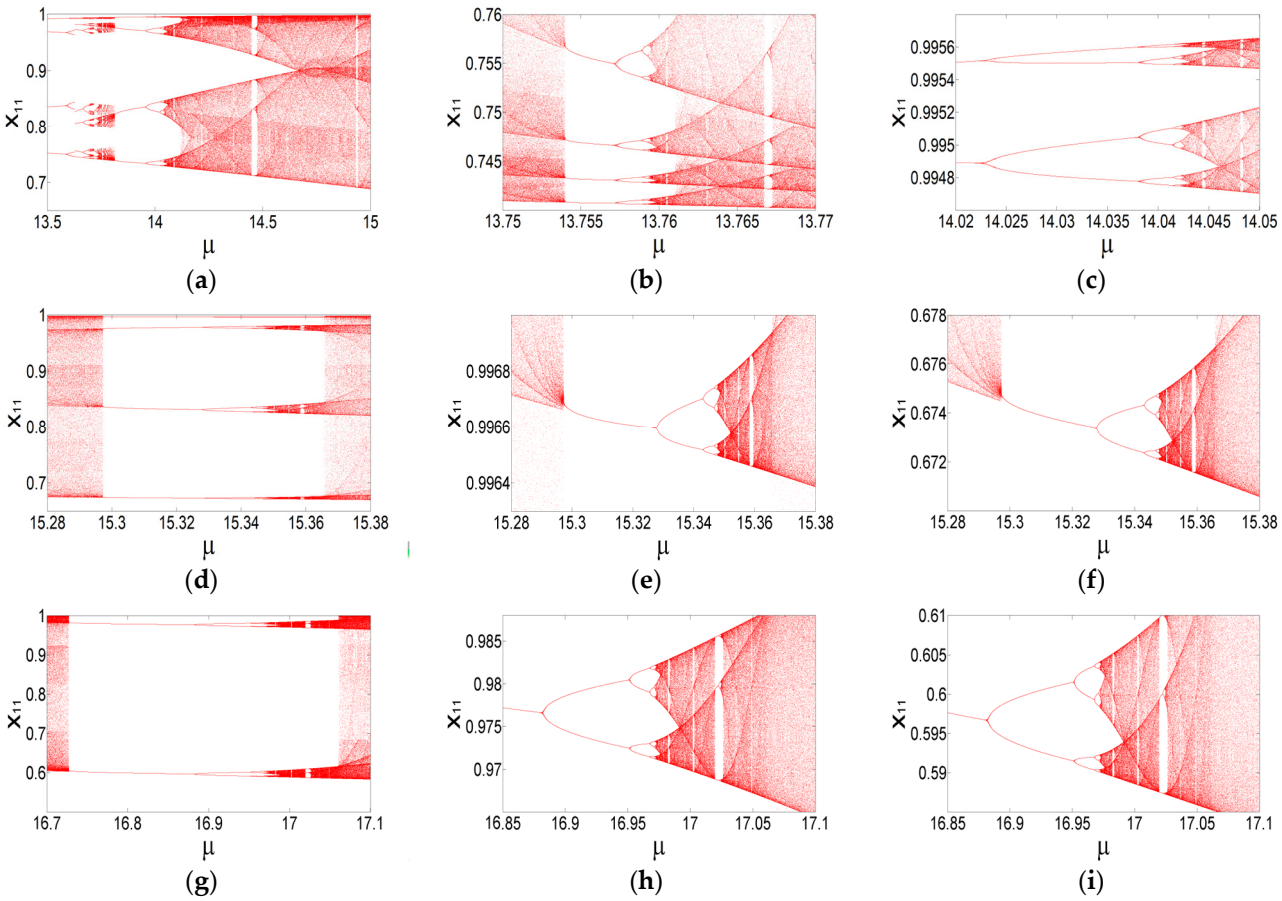


Figure 3. Single-parameter bifurcation diagram: (**a**–**i**) the local bifurcation diagram of Model 2 for μ.

Dynamic analysis of the model reveals that for small values of μ, the model maintains a periodic state and exhibits significant resilience against external disturbances. Correspondingly, traffic flows smoothly, and vehicles move in an orderly manner. However, as μ increases, the model enters a wide range of chaotic regions. During this period, the operational state of the traffic model becomes unstable, making it susceptible to disturbances or changes in road conditions that may result in road paralysis.

4.2. Three-Parameter Bifurcation

As an analytical tool for understanding the dynamic behavior of traffic systems, the three-parameter bifurcation diagram provides system characteristics and facilitates more

efficient parameter selection. The three-parameter bifurcation diagrams of the dynamic gravity models are presented within the range of $\mu \in [2,5]$, $\beta \in [0.1, 0.5]$, and $\gamma \in [2,3]$, where the initial state is given by Equation (2) and other settings are as specified in Table 3. Distinct colors are employed to indicate the different periodic phases of the system, and the color bars on the right side of the diagram are labeled with numbers. The maximum value of the color bar is set to 200.

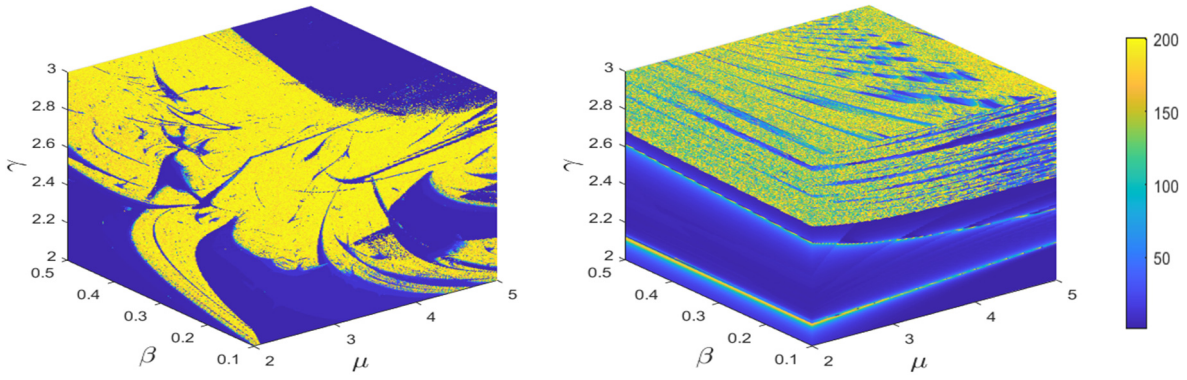
For a small γ, the surface of the cube in Figure 4a exhibits low periodicity and relatively stable motion characteristics. However, as γ increases, the system's low periodicity deteriorates, and larger areas of high and low periodicity emerge. This suggests that the system is prone to frequent transitions between chaotic states and periodicities, confirming its sensitivity in these regions. Figure 4b also illustrates a distinct boundary for $\gamma = 2.62$ between the yellow and blue sections. The lower part of the graph predominantly represents a low-period state, while the upper part is mainly occupied by a high-period state. Moreover, by adjusting μ, β, and γ within a certain range, the appropriate color area remains consistent within the yellow or blue regions. From a three-dimensional perspective, Model 2 appears to be more robust and stable.

Several cross-sections were selected to gain further insights. Comparing Figure 5a–c with Figure 5d–f reveals that for small γ, systems 1 and 2 are relatively stable and exhibit a dominant, strong, low-period state. Additionally, for larger values of $\gamma > 2.6$, systems 1 and 2 frequently alternate between high- and low-period states to varying degrees. This results in unpredictability in the traffic system and may compromise the smooth flow of road traffic. Therefore, if possible, such situations should be avoided in the design and optimization of roads.

From a three-dimensional perspective and based on the analysis of the cross-section sampling results, it can be observed that when the parameter γ is small, the systems appear to be more stable. However, when γ exceeds 2.6, the stability of the systems becomes highly complex, and it is impractical to determine the overall stability of the systems solely based on the cross-sectional sampling results. Subsequently, we employ the Hilbert curve dimensionality reduction technique to address this issue.

Table 3. Set of parameters in systems 1 and 2.

α	S_1	S_2	M
0.15	0.01	1.8	3



(**a**) (**b**)

Figure 4. The three-parameter bifurcation diagrams: (**a**) Model 1; (**b**) Model 2.

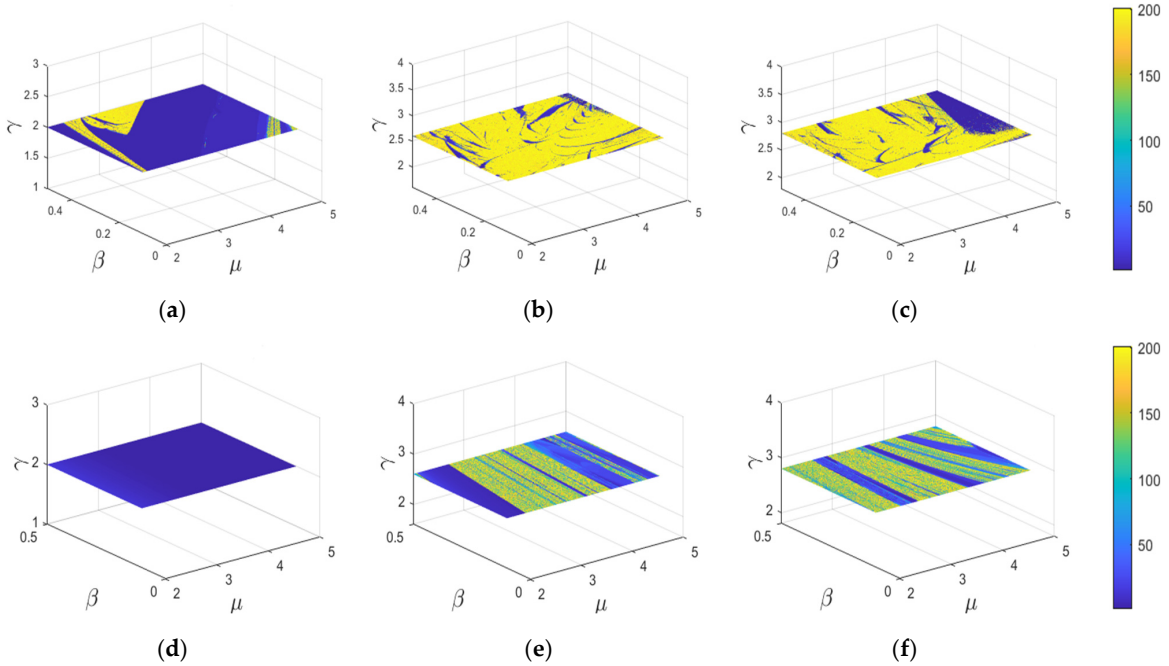


Figure 5. The cross-sections of the three-parameter bifurcation diagram: (**a**–**c**) $\gamma = 2,\ 2.6,\ 2.8$ (Model 1); (**d**–**f**) $\gamma = 2,\ 2.6,\ 2.8$ (Model 2).

5. Hilbert Curve

5.1. Two-Dimensional (Pseudo-)Hilbert Curves

Here, we describe the construction process of the two-dimensional Hilbert curve; as shown in Figure 6a, the first-order pseudo-Hilbert curve $G_1(t)$ is obtained in a clockwise or counterclockwise order. As shown in Figure 6b, the first-order curve is copied four times, a diagonal flip of the lower-left and lower-right curves is performed, and then three line segments are added to connect these four copies to obtain the second-order pseudo-Hilbert curve $G_2(t)$. By analogy, a sequence of curves $G_1(t)$,$G_2(t)$, ……, $G_n(t)$ can be obtained. When $n \to \infty$ tends to infinity, the points in the pseudo-Hilbert curve converge, $G(t) = \lim_{n\to\infty} G_n(t)$, and we obtain a complete two-dimensional Hilbert curve. Hilbert curves are a class of curves with a fractal structure that can pass through all of the points in space without repetition and retain the continuity of the original points as much as possible, exhibiting clear self-similarity, ergodicity, reversibility, and other characteristics.

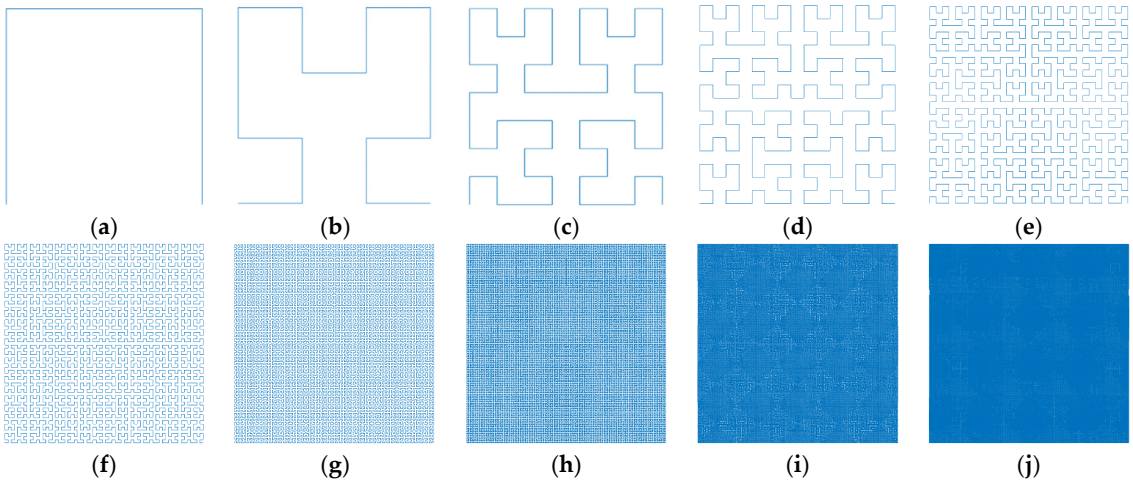


Figure 6. Two-dimensional nth-order pseudo-Hilbert curves: (**a**) $n = 1$; (**b**) $n = 2$; (**c**) $n = 3$; (**d**) $n = 4$; (**e**) $n = 5$; (**f**) $n = 6$; (**g**) $n = 7$; (**h**) $n = 8$; (**i**) $n = 9$; (**j**) $n = 10$.

5.2. Three-Dimensional (Pseudo-)Hilbert Curves

The spatial structure of the curve becomes more complex with the increase in dimensions. To clearly describe the characteristics of three-dimensional Hilbert curves, we adopt recursive and coding forms to depict the generation process of three-dimensional Hilbert curves based on the fractal properties of Hilbert curves.

A complete set of spatial state diagrams $\{\omega_1, \omega_2, \ldots\ldots, \omega_{12}\}$ of three-dimensional first-order pseudo-Hilbert primary curves is given, as shown in Figure 7. Each state comprises starting and ending points, both situated on the same side of the curve. The three-dimensional nth-order pseudo-Hilbert curve is denoted as $G(J, n)$, which is iteratively generated by any state J in the set of primary curves as the lowest-order pseudo-Hilbert curve.

The process of generating a pseudo-Hilbert curve is described here in the form of an encoding, which consists of a set of ordered numbers on a spatial grid. The pseudo-Hilbert encoding is expressed as

$$Hilbertcode = h_n h_{n-1} \ldots h_{i+1} h_i h_{i-1} \ldots h_1,$$

Each subcode, denoted as h_i, is derived based on the grid x_i, y_i, z_i and the corresponding state J. Table 4 represents the subcode h_i to which the function $f_{[\omega_1]}(x_i, y_i, z_i)$ maps the subcoordinates x_i, y_i, and z_i, corresponding to the pseudo-Hilbert curve $G(\omega_1, 1)$.

Table 4. Map of $G(\omega_1, 1)$.

x_i	y_i	z_i	h_i
0	0	0	1
0	0	1	2
0	1	1	3
0	1	0	4
1	1	0	5
1	1	1	6
1	0	1	7
1	0	0	8

With the shape of the primary curve shown in Figure 7, the mapping functions of the other primary curves are denoted as $\Phi_{[\omega_2]}(x_i, y_i, z_i), \ldots\ldots, \Phi_{[\omega_{12}]}(x_i, y_i, z_i)$ and can be derived by $\Phi_{[\omega_1]}(x_i, y_i, z_i)$; for example,

$$\Phi_{[\omega_2]}(x_i, y_i, z_i) = \Phi_{[\omega_1]}(z_i, x_i, y_i),\ \Phi_{[\omega_3]}(x_i, y_i, z_i) = \Phi_{[\omega_1]}(y_i, z_i, x_i).$$

The generation of Hilbert curves is a recursive process, meaning a curve of order n can be generated by a primary curve $G(J, 1)$ with a space size of $2^{n-1} \times 2^{n-1} \times 2^{n-1}$. Here, the function φ is provided for generating higher-order curves. Table 5 shows the mapping relationship of function φ. The corresponding Hilbert subcode $h_{i+1}(v)$ and the state J_{i+1} are input into the function φ to obtain J_i, where v represents the curve vertex. Then, connecting the curves along the curve direction of $G(J, n)$ generates a pseudo-Hilbert curve of a higher order. The generation process of Hilbert coding is described here by the following equation:

$$\begin{gathered} h_n = \Phi_{[J_n]}(x_n, y_n, z_n),\ J_n \in \{\omega_1 \omega_2 \ldots \omega_{12}\} \\ h_{n-1} = \Phi_{[J_{n-1}]}(x_{n-1}, y_{n-1}, z_{n-1}),\ J_{n-1} = \varphi(J_n, h_n) \\ \ldots \\ h_i = \Phi_{[J_i]}(x_i, y_i, z_i), J_i = \varphi(J_{i+1}, h_{i+1}) \\ \ldots \\ h_1 = \Phi_{[J_1]}(x_1, y_2, z_3), J_1 = \varphi(J_2, h_2) \end{gathered}$$

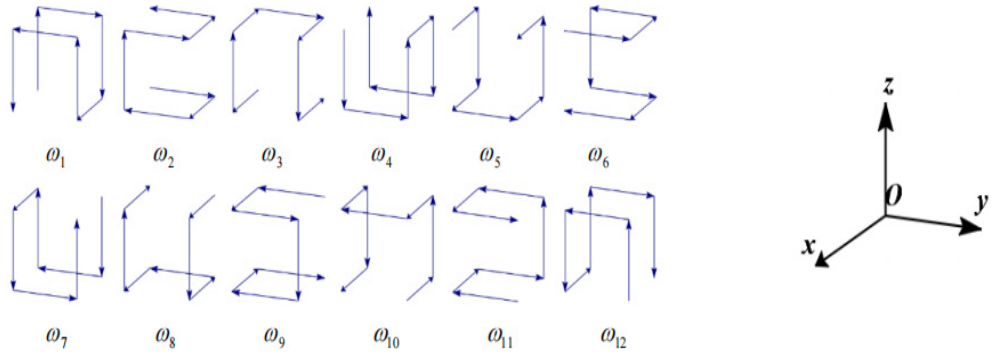


Figure 7. Three-dimensional 1st-order pseudo-Hilbert primary curves in space state diagrams.

Table 5. Map of $J_i = \varphi(J_{i+1}, h_{i+1})$.

S_{i+1} \ h_{i+1}	1	2	3	4	5	6	7	8
ω_1	ω_2	ω_3	ω_3	ω_{12}	ω_{12}	ω_5	ω_5	ω_9
ω_2	ω_3	ω_1	ω_1	ω_6	ω_6	ω_7	ω_7	ω_{10}
ω_3	ω_1	ω_7	ω_7	ω_8	ω_8	ω_{11}	ω_{11}	ω_4
ω_4	ω_6	ω_5	ω_5	ω_7	ω_7	ω_3	ω_3	ω_{11}
ω_5	ω_4	ω_6	ω_6	ω_{10}	ω_{10}	ω_9	ω_9	ω_1
ω_6	ω_5	ω_4	ω_4	ω_2	ω_2	ω_{12}	ω_{12}	ω_8
ω_7	ω_9	ω_8	ω_8	ω_4	ω_4	ω_{10}	ω_{10}	ω_2
ω_8	ω_7	ω_9	ω_9	ω_3	ω_3	ω_6	ω_6	ω_{12}
ω_9	ω_8	ω_7	ω_7	ω_{11}	ω_{11}	ω_1	ω_1	ω_5
ω_{10}	ω_{12}	ω_{11}	ω_{11}	ω_5	ω_5	ω_2	ω_2	ω_7
ω_{11}	ω_{10}	ω_{12}	ω_{12}	ω_9	ω_9	ω_4	ω_4	ω_3
ω_{12}	ω_{11}	ω_{10}	ω_{10}	ω_1	ω_1	ω_8	ω_8	ω_6

6. Three-Parameter Bifurcation Data Dimensionality Reduction

6.1. Conversion of Three-Dimensional Space Data into One-Dimensional Time Series

As indicated by the three-parameter bifurcation diagram and its cross-sectional information, when the parameter β is large, the dynamical behaviors of the systems become unstable, and high-period states are frequent, making it difficult to accurately compare and analyze the stability of the old and new systems from a global perspective. Therefore, we traverse the three-parameter bifurcation data by utilizing the three-dimensional sixth-order pseudo-Hilbert curve (Figure 8f) to reduce the bifurcation data from three dimensions to one dimension, as illustrated in Figure 9.

As depicted in Figure 9a, the periodic data oscillate frequently as t increases, indicating that the original system exhibits obvious periodic fluctuations in motion with variations in parameters α, β, and γ, and the dynamical behavior is extremely rich. Figure 9b illustrates that the periodic data are generally low in the interval $t \in [1,\ 130,000]$ and highly fluctuating in the interval $t \in [130,000,\ 262,144]$. This suggests that the new system primarily switches between low-period states as t increases, and, eventually, the periodicity becomes unstable, fluctuating frequently between high- and low-period states. Due to the pseudo-random nature of chaos, the upper limit of the period is set to 200 during the computation of the three-parameter bifurcation diagram. In fact, the periodic oscillations of the system in the interval $t \in [130,000,\ 262,144]$ are even more drastic than those shown in Figure 9. Because the set of one-dimensional time series is too long, we use the wavelet transform here to analyze it in depth.

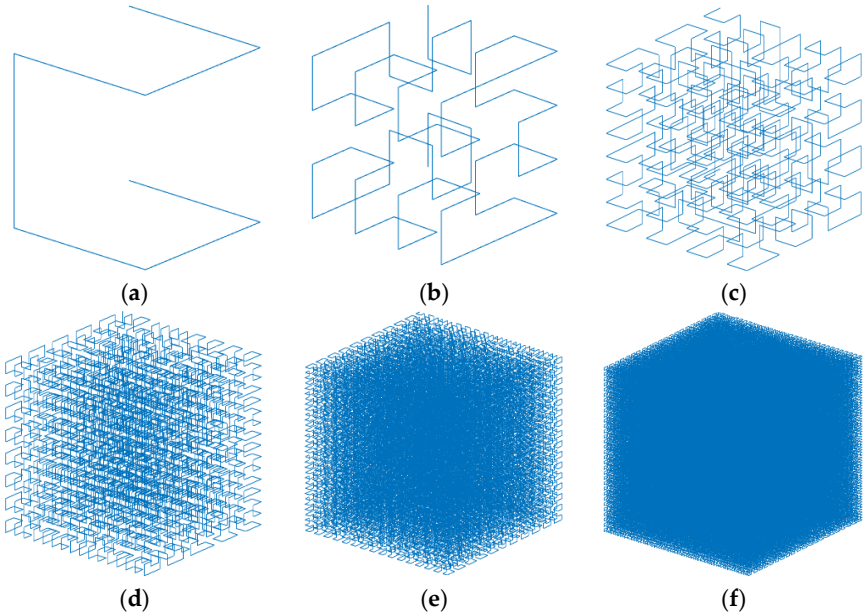


Figure 8. Three-dimensional nth-order pseudo-Hilbert curve: (**a**) $n = 1$; (**b**) $n = 2$; (**c**) $n = 3$; (**d**) $n = 4$; (**e**) $n = 5$; (**f**) $n = 6$.

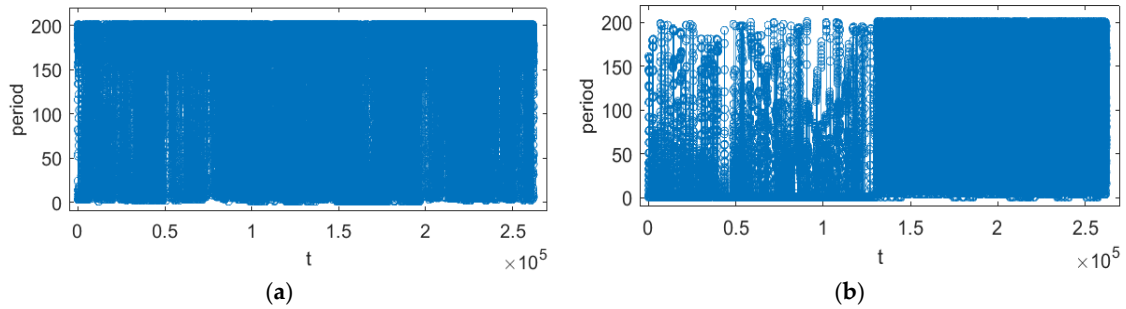


Figure 9. Three-dimensional bifurcation data reduced to one-dimensional data: (**a**) Model 1; (**b**) Model 2. The circles represent data.

6.2. Wavelet Transform for One-Dimensional Data

The wavelet transform involves the inner product of a square-integrable function $g(t)$ and a wavelet function $\tau(t)$ with well-localized properties in both the time and frequency domains.

$$W_g(d,e) = < g, \tau_{d,e} > = \frac{1}{\sqrt{d}} \int_{-\infty}^{+\infty} g(t)\tau^*(\frac{t-e}{d})dt,$$

where $<,>$ denotes the inner product, $d > 0$ is the scale factor, e is the displacement factor, $*$ denotes the complex conjugate, and $\tau_{d,e}(t)$ is referred to as the wavelet.

$$\tau_{d,e}(t) = \frac{1}{\sqrt{d}}\tau(\frac{t-e}{d}).$$

Changing the value of d has the effect of stretching ($d > 1$) or contracting ($d < 1$) the function $\tau_{d,e}(t)$; changing e affects the analytical results of the function $g(t)$ around the point e. $\tau(t)$ is called the mother wavelet, which must satisfy the following permissibility condition:

$$\int_{-\infty}^{+\infty} \tau(t)dt = 0 \text{ or } \int_{-\infty}^{+\infty} \frac{|\psi(\omega)|^2}{|\sigma|}d\sigma = C_\psi < \infty,$$

where $\tau(t)$ is the Fourier transform of $\psi(t)$.

Here, we select the Morlet wavelet

$$\tau(t) = \exp(i\sigma_0 t)\exp(-\frac{t^2}{2})$$

as the mother wavelet, where σ_0 is the center frequency.

Figure 10 displays the three-dimensional time–frequency diagrams of one-dimensional bifurcated data after wavelet transform. These diagrams result from the wavelet transform applied to the data presented in Figure 9a,b, elucidating additional system properties. The peaks illustrated in Figure 10 represent locations where various wavelet functions applied to one-dimensional data exhibit the highest energy at specific times and frequencies. Analyzing these peaks facilitates the identification of periodic or sudden events within the signal and unveils the frequency characteristics, along with their temporal change patterns. In Figure 10a, the changes in peaks are highly conspicuous, and the one-dimensional signal is abundant with numerous abrupt change points evenly distributed throughout the interval. In Figure 10b, the corresponding peak variation at $t \in [1,\ 130,000]$ is smoother than that at $t \in [130,000,\ 262,144]$, indicating that this one-dimensional signal contains significantly fewer mutation points in the early part of the period compared to the later part.

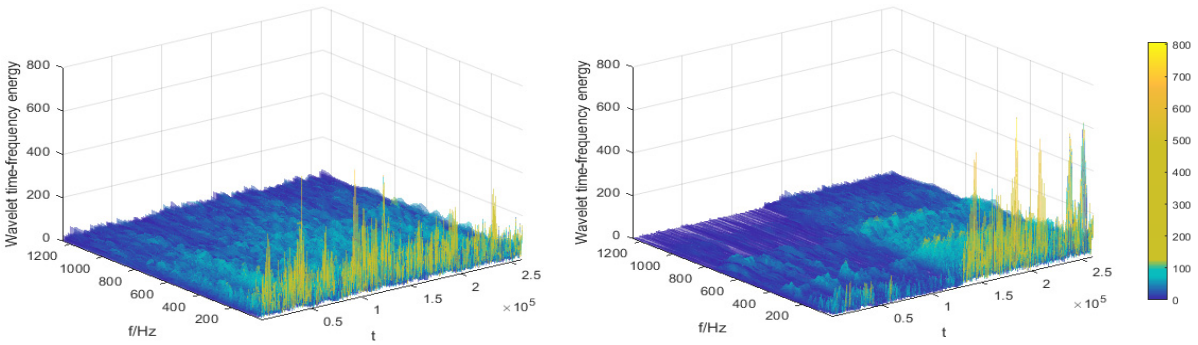


Figure 10. Three-dimensional time–frequency maps of the wavelet transform of one-dimensional bifurcation data: (**a**) Model 1; (**b**) Model 2.

Figure 11 shows the projection of the one-dimensional wavelet-transformed three-dimensional time–frequency map of one-dimensional bifurcation data onto the two-dimensional time–frequency plane. By enlarging Figure 11a,b to obtain Figure 11c,d, we can observe clearer signal mutation points, allowing us to understand the risk diagnosis and prevention of the system. From Figure 11c,d, it is evident that the coverage of the yellow high-energy region of the original system increases after $t = 24,345$, and this part of the yellow region exhibits a discontinuous distribution, while the new system does not exhibit this behavior. This indicates that the traffic flow movement pattern of the original system is more susceptible to changes in system parameters in the period after $t = 24,345$.

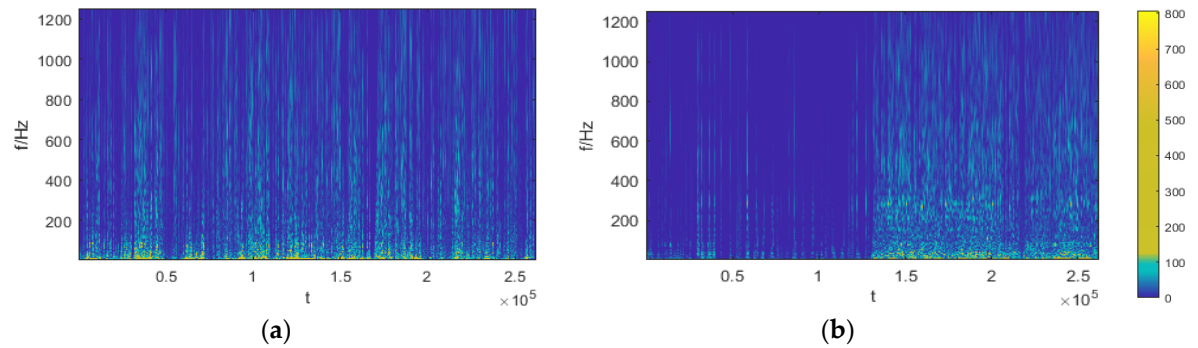


Figure 11. *Cont.*

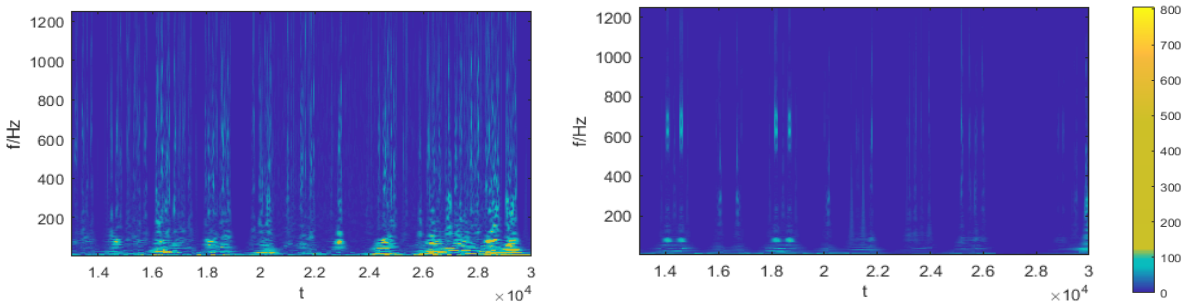


Figure 11. Time–frequency map of wavelet transform plane of one-dimensional bifurcation data: (**a**) Model 1; (**b**) Model 2; (**c**) localized enlargement of Model 1; (**d**) localized enlargement of Model 2.

6.3. Two-Dimensional Visualization and Analysis

The one-dimensional time series results in Figure 9 are mapped to each point on the two-dimensional ninth-order pseudo-Hilbert curve shown in Figure 6 and visualized with a cloud map to obtain the reduced-dimensional bifurcation diagram, as depicted in Figure 12. In this representation, the horizontal, vertical, starting, and ending coordinates are labeled as H_x, H_y, (0, 0), and (512, 0), respectively. Let $H_y = 55$.

From Table 6 and Figure 13, it can be observed that as H_x increases, the periodic regularity of the original system changes frequently, and chaotic phenomena occur at $H_x = 195$. At $H_x = 356$, with the increase in iteration number, the original system transitions from chaotic motion to period 9 motion, demonstrating transient chaotic phenomena. Subsequently, chaotic phenomena occur frequently and are accompanied by periodic phenomena. When H_x is small, the new system exhibits a very stable period 1 motion characteristic, while the value of x_{11} increases as H_x increases (Figure 13a–c). After $H_x = 356$, the time series of bifurcation data exhibits high-period motion as well as chaotic phenomena, indicating that the traffic flow generation law of the new system is more susceptible to changes in system parameters. As evident from Table 6, the original system shows a tendency of increased periodic oscillations and increased amplitude after $t = 24,345$, while this tendency is much less pronounced for the new system, which is consistent with the information reflected in Figure 11c,d.

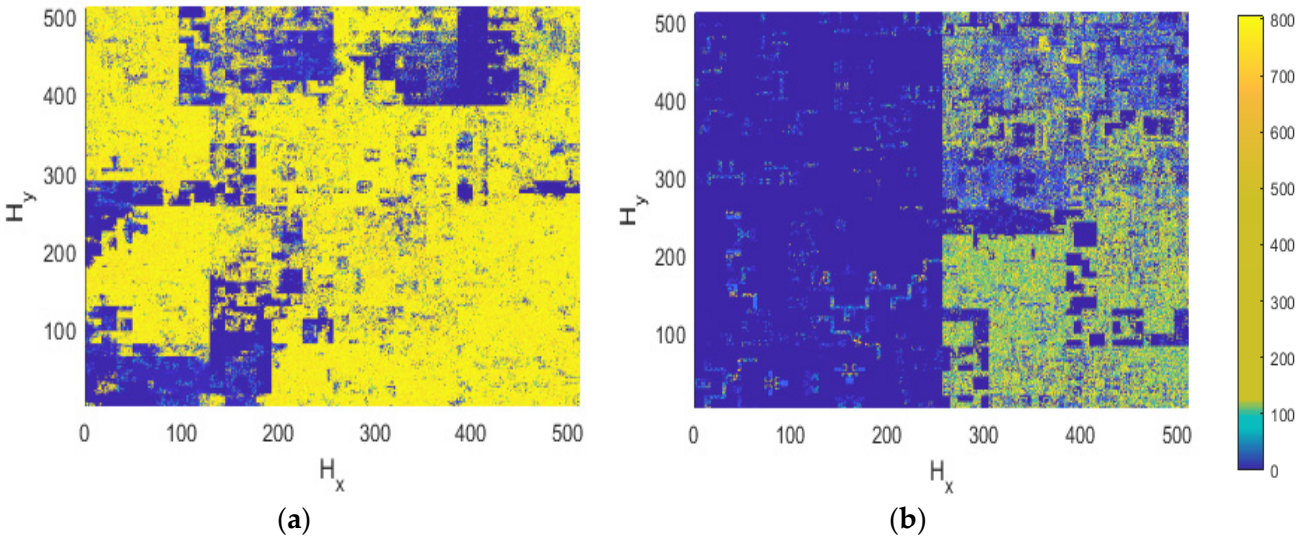


Figure 12. Bifurcation diagrams after two-dimensionalization of three-parameter bifurcation data: (**a**) Model 1; (**b**) Model 2.

Table 6. Correspondence between the relevant parameters and the systems state in Figure 12.

H_x	t	μ	β	γ	*Os*	*Ns*
72	13,700	2.8095	0.1190	2.0476	p-3	p-1
73	13,781	2.8571	0.1190	2.0794	p-6	p-1
162	18,750	3.0476	0.2905	2.1746	p-6	p-1
163	18,739	3.0476	0.2905	2.1270	p-3	p-1
195	24,345	2.8571	0.2714	2.3016	Chaos	p-1
197	24,357	2.8571	0.2651	2.254	p-6	p-1
201	24,445	2.9524	0.2714	2.2698	chaos	p-1
353	244,029	3.0476	0.2016	2.8254	p-10	p-66
356	244,020	3.0476	0.2079	2.8571	Chaos/p-9	p-29
440	248,364	2.8571	0.1190	2.9206	chaos	p-15
442	248,446	2.8095	0.1127	2.9524	chaos	chaos
443	248,435	2.8095	0.1127	3.0000	p-18	p-167
447	248,425	2.9048	0.1190	2.9841	p-10	p-127
449	259,479	2.5714	0.1952	2.8095	chaos	p-95
451	259,475	2.6190	0.1952	2.7937	p-194	p-31
453	259,469	2.6667	0.1889	2.7937	p-195	p-15
457	259,541	2.6190	0.1635	2.8095	p-14	p-5
459	259,545	2.6667	0.1698	2.8095	p-12	p-150
460	259,548	2.6667	0.1698	2.7937	p-78	p-24
503	258,179	2.2381	0.1063	2.8254	p-186	p-25

Os and *Ns* denote the periodic states of the original and new systems, respectively. 'p-number' is an abbreviation for 'period-number'.

Overall, the yellow color in Figure 12a predominates, indicating a propensity for the original system to undergo long-term high-period motion when parameters are altered, often leading to chaotic behavior. In contrast, Figure 12b reveals that the yellow area is primarily concentrated in the right half and appears lighter, while the left side is predominantly covered in blue. This suggests that the new system exhibits a greater prevalence of low-period states than the original system when parameters are modified, resulting in a significantly reduced likelihood of chaotic occurrences. Following the analysis conducted above, it is evident that the new system demonstrates stronger robustness when compared with the original system.

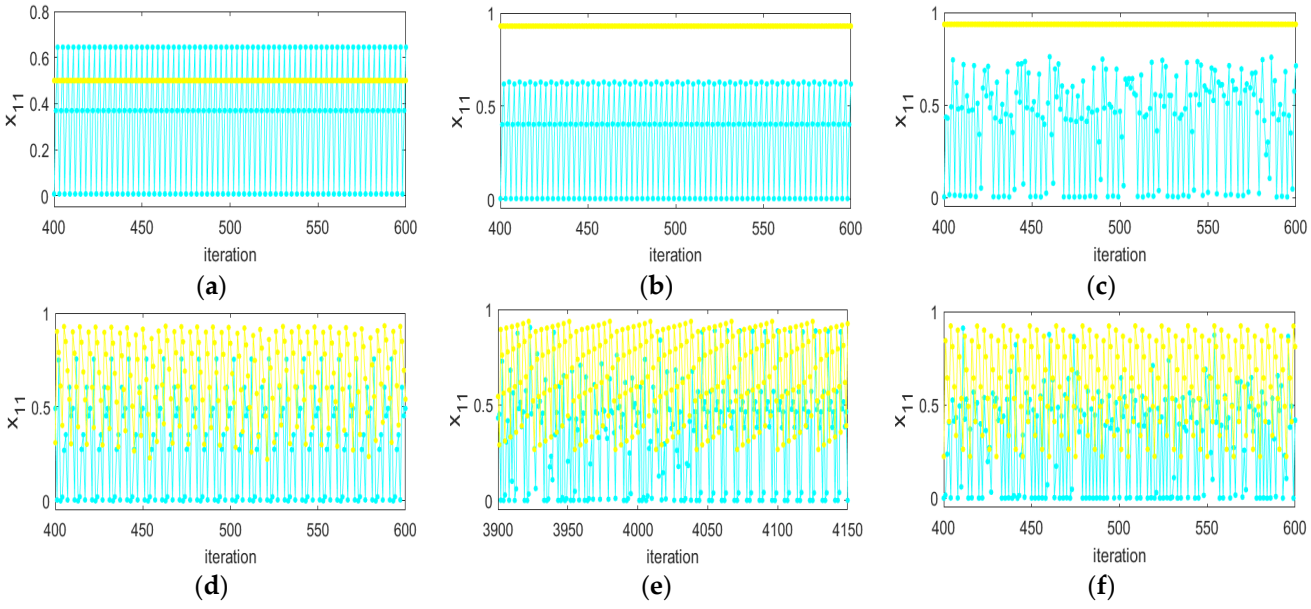


Figure 13. *Cont*.

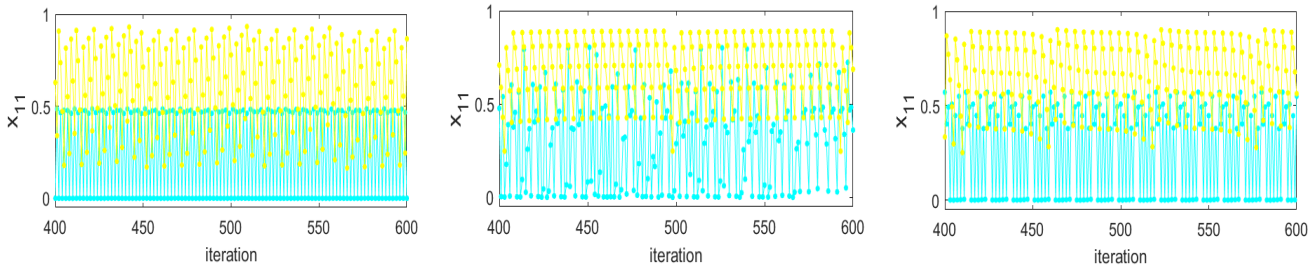


Figure 13. The data in Table 6 correspond to the time series: (**a**) $H_x = 72$; (**b**) $H_x = 162$; (**c**) $H_x = 201$; (**d**) $H_x = 353$; (**e**) $H_x = 356$; (**f**) $H_x = 440$; (**g**) $H_x = 447$; (**h**) $H_x = 449$; (**i**) $H_x = 459$. Blue solid points represent data from Model 1 and yellow solid points represent data from Model 2.

7. A Novel Robustness Evaluation Index

In this study, we investigated the motion patterns of the system under various saturation levels. For saturation thresholds S_1, S_2, and M, we define $N_\chi^\eta(\delta)$ as the count of points with a system period greater than or equal to num by traversing the parameter space $(\alpha - \beta - \gamma - \mu)$, where $\eta = \{\alpha, \beta, \gamma, \mu\}$ represents the set of non-saturation parameter thresholds for the system, $\delta = \{S_1, S_2, M\}$ represents the set of saturation parameter thresholds for the system, and χ is the periodic condition $periodic \geq num$.

For the cases where the origin is (2), $\alpha = 0.15$, and the other parameter settings are as listed in Table 7, the corrective system stability with different saturation thresholds is illustrated in Figure 14.

Table 7. Set of parameters in Model 2.

Parameter	Starting Point	Finishing Point	Step Length
β	0.1	0.5	0.01
γ	2	3	0.05
μ	2	5	0.1
S_1	0.1	0.9	0.1
S_2	1.1	1.9	0.1
M	2.6	3.4	0.1

In Figure 14, the x-, y-, and z-axes represent S_1, S_2, and $N^\eta_{periodic \geq 200}(\delta)$, respectively, and $N^\eta_{periodic \geq 200}(\delta)$ is abbreviated as $N_{P \geq 200}$. To highlight the effect of parameter M, all points with $N_{P \geq 200} \geq 4500$ are marked as solid yellow. The following important insights can be obtained regarding saturation parameters S_1, S_2, and M in Figure 14:

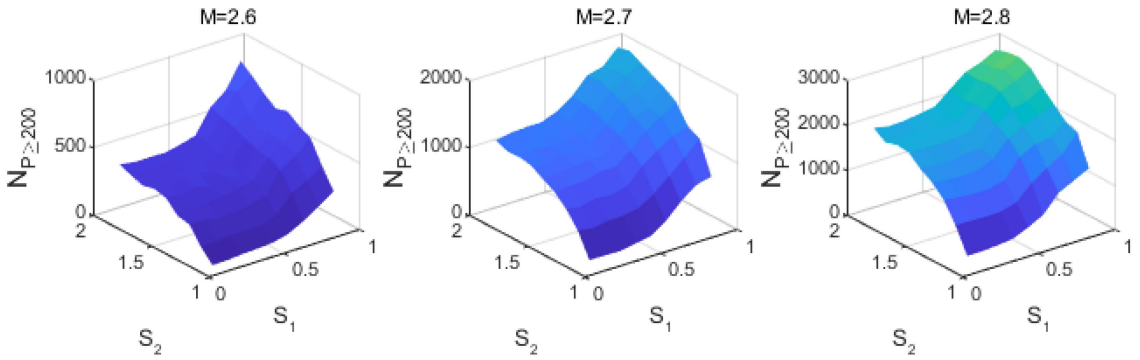


Figure 14. *Cont.*

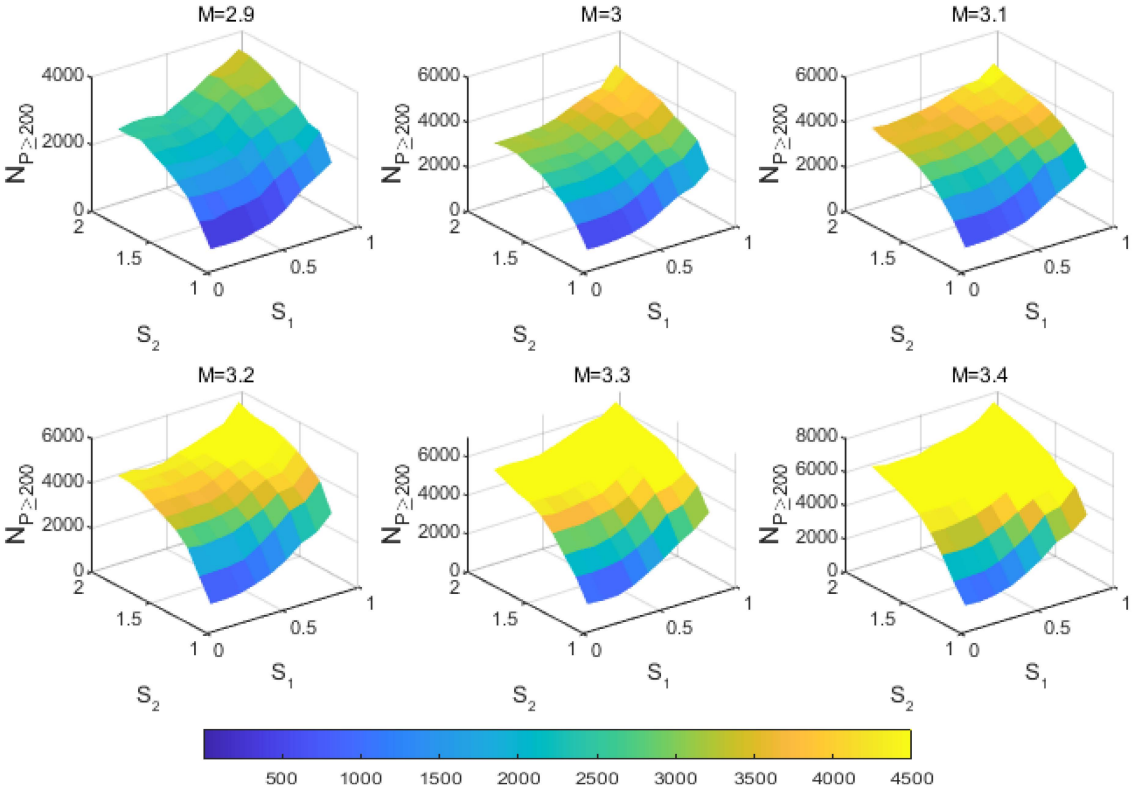


Figure 14. The surface graph of the robustness evaluation index $N_{P\geq 200}$ based on the dynamic stability.

1. For small values of S_1, the surface variation is imperceptible, but if its value exceeds a certain threshold (e.g., $S_1 > 0.3$), the magnitude of the surface variation increases significantly. In fact, under minimal traffic flows, vehicles operate almost freely, resulting in stable road conditions. However, increasing the flow beyond a specific threshold alters the stable traffic state, causing the system to exhibit diverse characteristics.

2. As S_2 increases, the surface also demonstrates a clear upward trend. The traffic system tends to become unstable when the traffic flow approaches the actual road capacity. The higher the actual capacity, the greater the level of instability.

3. For small values of M, the surface appears darker, and as M increases, both the height of the surface and the yellow area significantly increase, indicating a lower level of traffic system stability. Furthermore, the operating state of the traffic system during congestion is largely determined by the maximum saturation threshold M for different roads. Hence, increasing the maximum saturation level also increases the maximum travel cost. Expanding roads does not necessarily guarantee smoother operation of the road network. In cases where road traffic flow is oversaturated, the system quickly becomes unstable and may even reach a chaotic state.

8. Conclusions

From a saturation perspective, the original cost function is enhanced to make the modified gravity model suitable for calculating and analyzing traffic flow under unsaturated, saturated, and oversaturated traffic conditions. The three-parameter bifurcation data are two-dimensionalized using the Hilbert curve dimensionality reduction technique to analyze the dynamical behavior of the model from a new perspective. This study yields the following innovations and insights:

(1) The gravity model using the modified cost function exhibits the same rich dynamic behavior as the original model, including certain features, such as doubly periodic bifurcation, chaos, and fractals. Therefore, it can be used to study the distribution of road traffic OD flows. By comparing and analyzing the three-parameter bifurcation diagrams of the gravity systems, it is confirmed that the modified gravity model has stronger stability.

(2) A process-reversible Hilbert curve dimensionality reduction technique is proposed. Through the three-parameter bifurcation data reduction process of the gravity model, it can be seen that this dimensionality reduction technique is able to completely retain the data characteristics before the reduction, further enhance the degree of visualization of the high-dimensional data, and improve the technical means of parameter analysis in the engineering field. In addition, the wavelet transform is used to analyze the mutation points generated in the dimensionality reduction process, which further verifies the rationality of this reduction process of the data.

(3) A new robustness evaluation index is defined according to the dynamics of the model, and the simulation results reveal the strong relationship between the saturation parameter and road congestion. As the values of the saturation parameter thresholds S_1, S_2, and M increase, the corresponding values of the robustness indexes also increase, and the stability of the transportation system gradually decreases. Considering the sustainable operation of the road network, the saturation parameter thresholds should be controlled as much as possible to be not too large in the road network construction process.

With the continuous development of the economy, the demand for road transportation shows a trend of rapid growth. Various factors, such as accelerated urbanization, population increase, and a higher penetration of automobiles, have led to increasing pressure on road traffic. At the same time, the increase in logistics transportation and commercial activities has also put forward higher requirements for road reliability and efficiency. In the face of this status situation, today's traffic management model is facing a great challenge. Traditional traffic planning and management methods are often unable to meet the rapidly changing traffic demands and complex traffic environment. Problems, such as traffic congestion, traffic accidents, and environmental pollution, are becoming increasingly more prominent, thus negatively affecting the sustainable development of cities and the quality of life of residents.

In order to cope with these challenges, innovative traffic management models and technical means are needed. The Hilbert dimensionality reduction technique has unique advantages in the analysis of dynamical properties of multi-parameter models, including simple principles, reversible processes, and a high degree of visualization, which makes it unique among the dimensionality reduction techniques. By drawing the multi-parameter bifurcation diagram of the system in advance and matching the actual parameters of the system calibration with it, the stability level of the system can be quickly assessed, thus greatly reducing the time for managers to make decisions. Meanwhile, a method that is efficient and easy to propagate for analyzing the dynamic behavior of roads and developing saturation thresholds applicable to different types of roads is of great significance for the establishment of a sustainable early warning mechanism for road congestion.

Author Contributions: Conceptualization, L.Y., R.H. and J.W.; Methodology, L.Y., R.H. and J.W.; Software, L.Y., H.Z. and H.C.; Validation, L.Y., R.H. and J.W.; Formal analysis, L.Y.; Resources, L.Y., H.Z. and H.C.; Writing—original draft, J.W.; Writing —review & editing, L.Y. and R.H.; Visualization, L.Y.; Funding acquisition, L.Y. and R.H. All authors have read and agreed to the published version of the manuscript.

Funding: This research was funded by National Nature Science Foundation of China, grant number 52162041 and 71961015; Young Scholars Science Foundation of Lanzhou Jiaotong University, grant number 2021035.

Data Availability Statement: Data is contained within the article.

Conflicts of Interest: The authors declare no conflict of interest.

References

1. Angelidis, A.K.; Goulas, K.; Bratsas, C.; Makris, G.C.; Hanias, M.P.; Stavrinides, S.G.; Antoniou, I.E. Distinction of chaos from randomness is not possible from the degree distribution of the visibility and phase space reconstruction graphs. *Entropy* **2024**, *26*, 341. [CrossRef] [PubMed]
2. Wang, Y.L.; Jahanshahi, H.; Bekiros, S.; Bezzina, F.; Chu, Y.M.; Aly, A.A. Deep recurrent neural networks with finite-time terminal sliding mode control for a chaotic fractional-order financial system with market confidence. *Chaos Solitons Fractals* **2021**, *146*, 110881. [CrossRef]

3. Yao, G.; Liu, D. Aeroelastic stability analysis of a pyrotechnic separation plate in subsonic airflow. *Appl. Math. Model* **2022**, *107*, 574–590. [CrossRef]
4. Munch, S.B.; Rogers, T.L.; Johnson, B.J.; Bhat, U.; Tsai, C.H. Rethinking the prevalence and relevance of chaos in ecology, annual review of ecology evolution and systematics. *Annu. Rev. Ecol. Evol. Syst.* **2022**, *53*, 227–249. [CrossRef]
5. Yildiz, S.; Bilazeroglu, S.; Merdan, H. Stability and bifurcation analyses of a discrete Lotka-Volterra type predator-prey system with refuge effect. *J. Comput. Appl. Math.* **2023**, *422*, 114910. [CrossRef]
6. Bao, H.; Li, H.Z.; Hua, Z.Y.; Xu, Q.; Bao, B.C. Sine-transform-based memristive hyperchaotic model with hardware implementation. *IEEE Trans. Ind. Inform.* **2023**, *19*, 2792–2801. [CrossRef]
7. Nishioka, D.; Tsuchiya, T.; Namiki, W.; Takayanagi, M.; Imura, M.; Koide, Y.; Higuchi, T.; Terabe, K. Edge-of-chaos learning achieved by ion-electron-coupled dynamics in an ion-gating reservoir. *Sci. Adv.* **2023**, *8*, eade1156. [CrossRef] [PubMed]
8. Kengne, E.R.M.; Kammogne, A.S.T.; Tamo, T.T.; Azar, A.T.; Mahlous, A.R.; Ahmed, S. Photovoltaic systems based on average current mode control: Dynamical analysis and chaos suppression by using a non-adaptive feedback outer loop controller. *Sustainability* **2023**, *15*, 8238. [CrossRef]
9. Pacheco, P.; Mera, E.; Salini, G. Urban densification effect on micrometeorology in Santiago, Chile: A comparative study based on chaos theory. *Sustainability* **2022**, *14*, 2845. [CrossRef]
10. Wang, X.J.; Peng, M.S. Rich dynamics in some discrete-time car-following models. *Physica A* **2019**, *536*, 120926. [CrossRef]
11. Men, J.K.; Chen, G.H.; Chen, P.Z.; Zhou, L.X. A Gaussian type-2 fuzzy programming approach for multicrowd congestion-relieved evacuation planning. *IEEE Trans. Intell. Transp.* **2022**, *23*, 20978–20990. [CrossRef]
12. Ren, W.L.; Cheng, R.J.; Ge, H.X. Bifurcation analysis of a heterogeneous continuum traffic flow model. *Appl. Math. Model.* **2021**, *94*, 369–387. [CrossRef]
13. Wang, Y.; Zhang, Z.; Wei, H.; Yin, G.; Huang, H.; Li, B.; Huang, C. A novel fault-tolerant scheme for multi-model ensemble estimation of tire road friction coefficient with missing measurements. *IEEE Trans. Intell. Veh.* **2024**, *9*, 1066–1078. [CrossRef]
14. Zhang, Z.; Yang, Y. Time pattern recognition of traffic flow in terminal area based on community division. *Mob. Netw. Appl.* **2022**, *27*, 2543–2552. [CrossRef]
15. Fang, Y.L.; Shi, Z.K. Chaos analysis and delayed-feedback control in a discrete dynamic coupled map traffic model. *Physica A* **2015**, *422*, 40–46. [CrossRef]
16. Krese, B.; Govekar, E. Analysis of traffic dynamics on a ring road-based transportation network by means of 0–1 test for chaos and Lyapunov spectrum. *Transp. Res. C-Emer.* **2013**, *36*, 27–34. [CrossRef]
17. Tian, Z. Chaotic characteristic analysis of network traffic time series at different time scales. *Chaos Solitons Fractals* **2020**, *130*, 109412. [CrossRef]
18. Zhang, Z.; Zhang, A.; Sun, C.; Xiang, S.; Li, S. Data-driven analysis of the chaotic characteristics of air traffic flow. *J. Adv. Transp.* **2020**, *2020*, 8830731. [CrossRef]
19. Li, Y.; Jiang, X.; Zhu, H.; He, X.; Peeta, S.; Zheng, T.; Li, Y. Multiple measures-based chaotic time series for traffic flow prediction based on Bayesian theory. *Nonlinear Dyn.* **2016**, *85*, 179–194. [CrossRef]
20. Murat, C.H. Sample size needed for calibrating trip distribution and behavior of the gravity model. *J. Transp. Geogr.* **2010**, *18*, 183–190. [CrossRef]
21. Simini, F.; González, M.C.; Maritan, A.; Barabási, A. A universal model for mobility and migration patterns. *Nature* **2012**, *484*, 96–100. [CrossRef] [PubMed]
22. Hong, I.; Jung, W.S. Application of gravity model on the Korean urban bus network. *Phys. A Stat. Mech. Appl.* **2016**, *462*, 48–55. [CrossRef]
23. Goh, S.; Lee, K.; Park, J.S.; Choi, M.Y. Modification of the gravity model and application to the metropolitan Seoul subway system. *Phys. Rev. E* **2012**, *86*, 026102. [CrossRef] [PubMed]
24. Wu, Z.; Huang, M.; Zhao, A.; Lan, Z. Urban traffic planning and traffic flow prediction based on ulchis gravity model and Dijkstra algorithm. *J. Phys. Conf. Ser.* **2021**, *2021*, 012080. [CrossRef]
25. Asmael, N.; Waheed, M. Demand estimation of bus as a public transport based on gravity model. *Matec Web. Conf.* **2018**, *162*, 01038. [CrossRef]
26. Zhang, X.Y.; David, F.J. Chaos in a dynamic model of traffic flows in an origin-destination network. *Chaos* **1998**, *8*, 503–513. [CrossRef] [PubMed]
27. Faradja, P.; Qi, G.Y. Analysis of multistability, hidden chaos and transient chaos in brushless DC motor. *Chaos Solitons Fractals* **2020**, *132*, 109606. [CrossRef]
28. Ayubi, P.; Barani, M.J.; Valandar, M.Y.; Irani, B.Y.; Sadigh, R.S.M. A new chaotic complex map for robust video watermarking. *Artif. Intell. Rev.* **2021**, *54*, 1237–1280. [CrossRef]
29. Choudhary, K.K.; Dubey, B. A non-autonomous approach to study the impact of environmental toxins on nutrient-plankton system. *Appl. Math. Comput.* **2023**, *458*, 128236. [CrossRef]
30. Duncan, D.; Räth, C. Optimizing the combination of data-driven and model-based elements in hybrid reservoir computing. *Chaos* **2023**, *33*, 103109. [CrossRef] [PubMed]
31. Fang, J.B.; Cu, W.K.; Liu, H.; Zhang, H.X.; Liu, H.Q.; Wei, J.J.; Ma, X.; Zheng, N. Data driven reduced modeling for fluidized bed with immersed tubes based on PCA and Bi-LSTM neural networks. *Particuology* **2024**, *91*, 1–18. [CrossRef]

32. Teng, Q.Y.; Zhou, K.K.; Yu, K.H.; Zhang, X.Y.; Li, Z.J.; Wang, H.F.; Zhu, C.Z.; Wang, Z.Y.; Dai, Z.H. Principal component analysis-assisted zirconium-based metal-organic frameworks/DNA biosensor for the analysis of various phosphates. *Talanta* **2024**, *271*, 125733. [CrossRef] [PubMed]
33. Li, Z.X.; Nie, F.P.; Wang, R.; Li, X.L. A revised formation of trace ratio LDA for small sample size problem. *IEEE Trans. Neural Netw. Learn. Syst.* **2024**. [CrossRef] [PubMed]
34. Lei, Y.; Tong, X.C.; Wang, D.L.; Qiu, C.P.; Li, H.; Zhang, Y.W. W-Hilbert: A W-shaped Hilbert curve and coding method for multiscale geospatial data index. *Int. J. Appl. Earth Obs. Geoinf.* **2023**, *118*, 103298. [CrossRef]
35. Dai, X.F.; Feng, W.J.; Che, W.Q. Implicit periodic strong reflection points of uwb Hilbert fractal time delay lines and the performance improvements. *IEEE Trans. Microw. Theory* **2022**, *70*, 4376–4388. [CrossRef]
36. Chen, J.F.; Yu, L.; Wang, W.Y. Hilbert space filling curve based scan-order for point cloud attribute compression. *IEEE Trans. Image Process.* **2022**, *31*, 4609–4621. [CrossRef] [PubMed]
37. Soltani-Kordshuli, F.; Miller, C.; Harris, N.; Zou, M. Laser surface texturing of both thin polytetrafluoroethylene coatings and stainless steel substrates for improving tribological properties. *Polym. Test.* **2023**, *117*, 107852. [CrossRef]
38. Yang, C.; Wang, Y.; Wang, Y.; Hu, D.Y.; Guo, H. An improved functional beamforming algorithm for far-field multi-sound source localization based on Hilbert curve. *Appl. Acoust.* **2022**, *192*, 108729. [CrossRef]
39. Jalayer, M.; Orsenigo, C.; Vercellis, C. Fault detection and diagnosis for rotating machinery: A model based on convolutional LSTM, Fast Fourier and continuous wavelet transforms. *Comput. Ind.* **2021**, *125*, 103378. [CrossRef]
40. Liu, K.L.; Cheng, J.H.; Yi, J.H. Copper price forecasted by hybrid neural network with Bayesian Optimization and wavelet transform. *Resour. Policy* **2022**, *75*, 102520. [CrossRef]
41. Liang, P.F.; Wang, W.H.; Yuan, X.M.; Liu, S.Y.; Zhang, L.J.; Cheng, Y.W. Intelligent fault diagnosis of rolling bearing based on wavelet transform and improved ResNet under noisy labels and environment. *Eng. Appl. Artif. Intell.* **2022**, *115*, 105269. [CrossRef]
42. Zhao, H.M.; Liu, J.; Chen, H.Y.; Chen, J.; Li, Y.; Xu, J.J.; Deng, W. Intelligent diagnosis using continuous wavelet transform and Gauss convolutional deep belief network. *IEEE Trans. Reliab.* **2023**, *72*, 692–702. [CrossRef]
43. Zheng, Y.; Du, Y.C.; Sun, L.J. Considerations on problems in the BPR function. *Traffic Transp.* **2007**, *23*, 24–26. (In Chinese)
44. Wang, S.X.; Wang, L.Z.; Gao, L.; Gui, X.G.; Chen, X.M. Improvement study on BPR link performance function. *J. Wuhan Univ. Technol.* **2009**, *33*, 446–449. (In Chinese) [CrossRef]

Disclaimer/Publisher's Note: The statements, opinions and data contained in all publications are solely those of the individual author(s) and contributor(s) and not of MDPI and/or the editor(s). MDPI and/or the editor(s) disclaim responsibility for any injury to people or property resulting from any ideas, methods, instructions or products referred to in the content.